Uptake, transport, and release of hydrogen from Pd(100)

W.D. Michalak [a,b], J.B. Miller [a,b], D.R. Alfonso [a], A.J. Gellman [a,b,*]

[a] U.S. Department of Energy, National Energy Technology Laboratory, Pittsburgh, PA 15236, United States
[b] Department of Chemical Engineering, Carnegie Mellon University, Pittsburgh, PA 15213, United States

ARTICLE INFO

ABSTRACT

Understanding the interactions of hydrogen atoms with the surface and the subsurface regions of Pd is critical to the development of advanced energy technologies for hydrogen storage, hydrogen separations, and catalytic conversion processes. While many of the physical and chemical characteristics of the H_2–Pd system are known, the kinetics and thermodynamics of H atom absorption into the bulk, transport from the bulk back to the surface, and desorption from the surface remain unclear. In this work, the kinetics of D_2 release from Pd following exposure to D_2 over a range of pressures and temperatures were measured using temperature programmed desorption. To accurately simulate the kinetics of D_2 release, the continuum-based model of Mavrikakis, et al. (J. Chem. Phys 105, 8398, 1996) was extended to include activation barriers for desorption and transport that depend on D atom concentration in the surface, subsurface and bulk regions of the Pd. The use of concentration dependent barriers improves the ability of the model to predict the hydrogen uptake and release kinetics observed across temperatures ranging from 100 to 600 K.

© 2011 Elsevier B.V. All rights reserved.

1. Introduction

The ability of metallic Pd to dissociate H_2 and absorb H atoms has led to its use in a number of important technologies, including H_2 separation, H_2 storage, and heterogeneous catalysis. However, despite years of experimental and computational study of the Pd–H system, many details of the atomic level interactions between Pd and H remain unclear. Only a few studies have combined first-principles calculations and experimental data to develop kinetic and thermodynamic models of hydrogen uptake, transport, and release from Pd; even fewer models can predict the behavior of the Pd–H system over a wide range of temperatures and concentrations [1]. A significant challenge to the development of such models is a complete understanding of pathways and energetics for H penetration into bulk Pd.

H-transport in solids is commonly described using a theoretical framework based on a set of mean-field reaction–diffusion equations. A historical perspective of the evolution of this approach is given by Pisarev et al. [2]. The most frequent application of this modeling scheme has been to describe H-permeation in separation membranes, storage devices, and nuclear reactor walls. Mean-field reaction–diffusion models customarily focus on either surface-limited or bulk-limited regimes depending on the temperature. For transport across a membrane, they stipulate equilibrium between H in the bulk metal and in the gas-phase (i.e. Sievert's law) and they typically describe the temporal and spatial H distribution in the bulk by assuming that the flux is directly proportional to the linear chemical potential (concentration) gradient across the membrane [1–6]. These assumptions are introduced because the nonlinear boundary conditions preclude an exact analytic solution to the system of equations governing the concentrations in the bulk. A shortcoming of these assumptions – particularly Sievert's law – is that they explicitly ignore the surface-bulk interface.

More detailed H transport models have been developed to model H uptake in hydrogen storage systems [7] and to replicate the transient kinetics of H release/desorption in Pd as observed in TPD experiments [8–10]. The range of desorption features observed in TPD studies illustrates the complexity of the phenomena that occur in H–Pd systems, and provides insight into the processes involved in the release of H. The different TPD desorption features include a low temperature desorption feature (between 130 K and 200 K depending on the heating rate and exposure) assigned to the decomposition of a 'near-surface phase of Pd hydride', a feature at ~250 K assigned to surface reconstruction and defect-induced desorption, a feature at ~300 K assigned to recombinative desorption of H atoms on the surface, and a high temperature feature assigned to H diffusion and release from the bulk [11–21]. A number of surface science studies have established that these desorption features are related to the exchange of H between three distinct regions: the surface, the immediate subsurface layer, and the bulk [11–14,16,18–21]. The importance of a distinct subsurface region is now a well-established feature of the H–Pd system and is considered an integral component of any model that describes the kinetics of H uptake and release at Pd surfaces. A schematic diagram of the H–Pd system, which defines the distinct regions of the Pd(100) system studied in this work (surface, subsurface, and bulk), appears in Fig. 1. The small blue, green, and orange spheres represent H atoms in the surface,
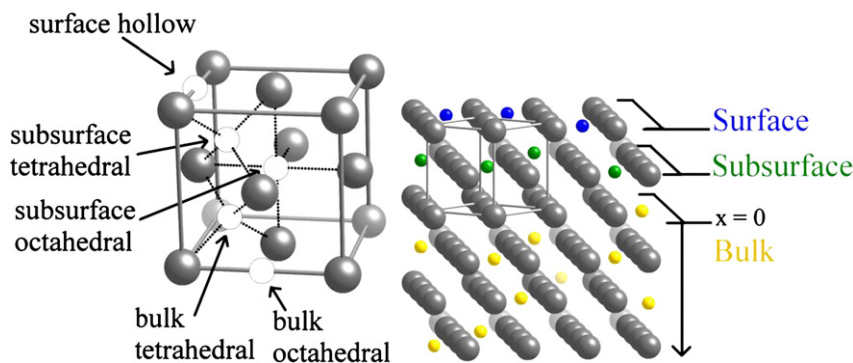

Fig. 1. Representative diagram for the simulated D–Pd system. The small blue, green, and orange atoms correspond to D in the surface (S), subsurface (SS), and bulk (B), respectively. The large gray atoms correspond to Pd which surrounds D. The enlargement of the unit cell illustrates the surface hollow, subsurface tetrahedral, subsurface octahedral, bulk tetrahedral, and bulk octahedral sites. The model assumes H only occupies hollow sites on the surface and octahedral sites in the subsurface and bulk.

subsurface, and bulk of Pd, respectively. The large gray spheres represent Pd atoms that surround H atoms. The enlargement of the fcc unit cell shows the locations of the surface four-fold hollow site, subsurface tetrahedral site, subsurface octahedral site, bulk tetrahedral site, and the bulk octahedral site. The tetrahedral sites are considered to be transient or metastable sites along the reaction pathway leading from the surface four-fold hollow to the subsurface octahedral site to the bulk octahedral site.

Mavrikakis et al. [8–10], using a mean-field modeling framework similar to that described by Pisarev [2], simulated the H–Pd(110) TPD experiment performed by Conrad et al. [11]. Three aspects distinguish Mavrikakis' approach from previous modeling efforts: a three-domain model including the surface, subsurface, and bulk regions; a consistent treatment of both isothermal exposure and heating stages of the experiment; and a numerical solution scheme involving a discrete element representation of the bulk domain.

The range of desorption features observed in TPD experiments for H_2 on Pd surfaces suggests that models that use constant barrier heights for the elementary steps cannot completely describe uptake into and release from Pd [12,21–23]. Discrepancies among transport mechanisms become particularly apparent when describing H uptake into the Pd bulk at temperatures <300 K. Many studies have attributed low-temperature transport into the subsurface to tunneling effects or to a separate reaction coordinate that directly links gas-phase H_2 to H atoms in subsurface sites; however, while energetically possible, such mechanisms have a low probability [24–26]. Transport into the bulk via minority defect sites is also a commonly proposed pathway [12–14,21]. More recently, first principles calculations have shown that H-induced distortion of the top few Pd layers influences the energetics of the H transport pathways into the bulk. These studies predict H-induced lateral distortion (intralayer relaxation) and plane-to-plane separation (interlayer relaxation) of the Pd lattice due to adsorption and absorption of H; these relaxations destabilize H at surface sites and stabilize H at subsurface sites, respectively [19,25,27,28]. Most of the existing models of H uptake and transport in Pd have been based on the use of kinetic parameters that are independent of the H concentration in the system thus, limiting their applicability to low concentration regimes. We believe that a kinetic model of H transport in Pd must account for concentration (H-occupation of the surface and subsurface) dependence of the kinetic parameters.

We have developed a model for hydrogen uptake, bulk transport, and release from Pd(100) that builds on and extends the work of Mavrikakis et al. [10] by incorporating activation barriers that depend on H-atom concentration in the various sites along the penetration pathways. A key feature of our simulations, which follows from Mavrikakis et al., is that all three experimental stages – exposure, cooling/evacuation, and temperature programmed heating – are incorporated into the model to eliminate the need for assumptions about the initial H atom

concentration distribution within the Pd prior to the TPD experiments. With the assumption that the H concentration in the Pd crystal is negligible before we initiate exposure to H_2, we allow the model to describe
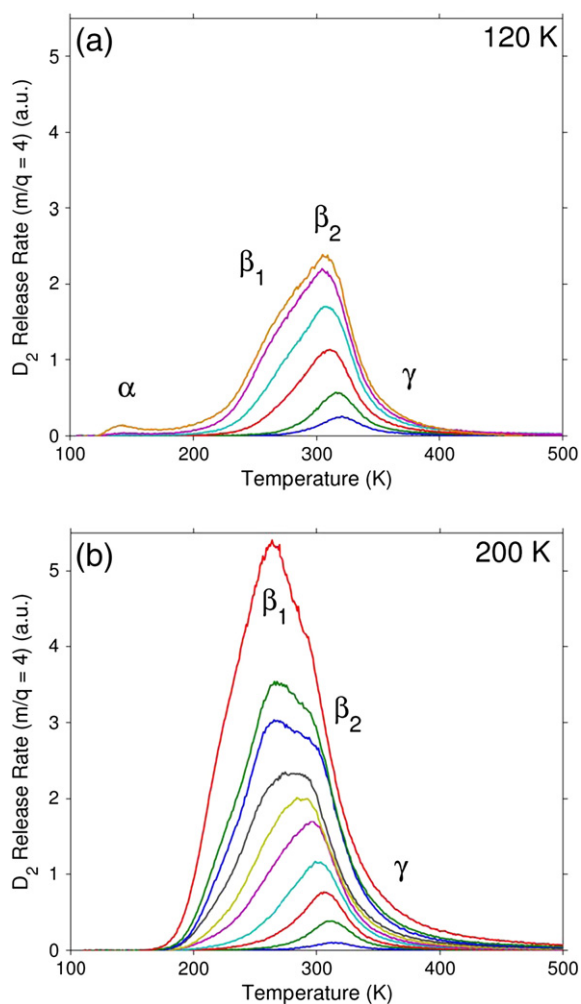

Fig. 2. Temperature programmed desorption (TPD) of D_2 ($m/q=4$) from Pd(100) monitored with a mass spectrometer. The spectra correspond to exposures performed for 100 s at (a) 120 K and (b) 200 K Pd sample temperatures. The pressures used in (a) are 8.5×10^{-10}, 2.0×10^{-9}, 1.14×10^{-8}, 1.43×10^{-7}, and 2.8×10^{-6} Torr; and in (b) 8.57×10^{-10}, 2.0×10^{-9}, 5.71×10^{-9}, 1.14×10^{-8}, 2.28×10^{-8}, 1.0×10^{-7}, 1.43×10^{-7}, 2.85×10^{-7}, and 1.42×10^{-6} Torr. The pressures were measured using an ion-gauge and normalized by D_2's relative sensitivity: 0.35. TPD measurements were initiated at 100 K and continued with a sample heating rate of 3 K/s. Four features are present in the figures: α, β_1, β_2 and γ.

both the uptake into and release of H from Pd. Using our own TPD results obtained for D_2 uptake and release from Pd(100), which were acquired over a range of exposure conditions, we illustrate the need to incorporate concentration dependent activation barriers into the model to accurately reproduce experimental observations.

2. Experimental methods

Temperature Programmed Desorption (TPD) experiments using D_2 on Pd(100) were performed in a stainless steel UHV chamber with a quadrupole mass spectrometer (QMS; Ametek Inc., Dycor 2000) to detect the desorbing D_2. The chamber is evacuated with a turbomolecular pump, a cryogenic pump, and a titanium sublimation pump to a base pressure of 1×10^{-9} Torr. The chamber is equipped with an X-ray photoelectron spectroscopy (XPS) system that we used for verification of the cleanliness of the Pd(100) crystal. XPS measurements were carried out with a hemispherical electrostatic energy analyzer (VG CLAM 2) and an X-ray source (SPECS/XRC-1000) operating at 20 mA with an Al anode at a 13 kV potential.

The Pd(100) single crystal was mounted, via Ta leads spot-welded to its edges, to an electrically isolated copper block that was in thermal contact with a liquid nitrogen reservoir. The sample was heated resistively by passing current directly through it via the Ta leads. The crystal temperature was measured with an alumel–chromel (K-type) thermocouple spot welded to its backside. This configuration allowed control of crystal temperature between 80 and 1400 K.

The surface of the Pd substrate was prepared outside the chamber by polishing it to a mirror finish using a sequence of fine grit SiC paper and Buehler METADI® diamond suspensions. Once inside the chamber, the surface was cleaned by 10-minute cycles of Ar^+ sputtering (1 kV), annealing at 1000 K, and oxidation in 10^{-7} Torr O_2 at 700 K. Cycles were repeated until the main contaminant, carbon, was removed, as confirmed by the absence of CO ($m/q = 28$) in the QMS desorption trace obtained during heating after exposure to O_2.

For the D_2 TPD experiments, the clean Pd(100) surface was exposed to D_2 (Matheson Tri Gas, research grade) introduced into the chamber via an external leak valve. D_2 adsorption was performed with the Pd(100) surface held at either 120 K or 200 K while exposing its surface to D_2 at pressures from 8.5×10^{-10} to 2.8×10^{-6} Torr for 100 s. In reaction–diffusion
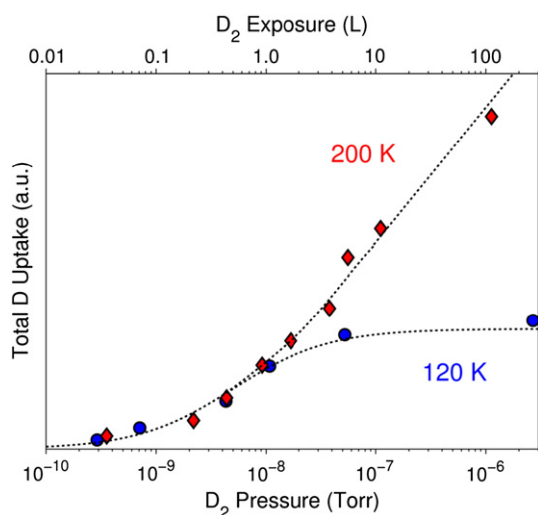

Fig. 3. Adsorption isotherms showing uptake (integral area under TPD profile) versus exposure (pressure during 100 s exposure) and equivalent L ($1L = 1 \times 10^{-6}$ Torr·s) for two exposure temperatures: 120 K and 200 K. The uptake is similar with increasing pressure until a breakpoint occurs, which coincides with near surface saturation. At this point there is a change in the rate limiting step for uptake (i.e. the uptake/sticking coefficient changes).

systems the pressure–time symmetry is broken [16], and therefore, reporting exposures in Langmuir ($1L = 10^{-6}$ Torr·s) can be misleading. At the end of the exposure, the Pd(100) sample was cooled to 100 K while the residual D_2 was evacuated from the chamber. TPD was performed by positioning the surface immediately in front of the aperture to the QMS and heating the surface from 100 to 700 K at 3 K/s. The rates of D_2 desorption were monitored by the QMS. We chose to use D_2 over H_2 to improve the signal-to-noise ratio of the TPD measurements and eliminate the possibility of overlap from H_2O ionization signals.

3. Experimental results

The kinetics of D adsorption, absorption, release and desorption from Pd(100) was studied by TPD following exposure of the Pd(100) surface to D_2 over a range of temperatures and pressures. TPD spectra acquired after exposing the Pd(100) single crystal to D_2 for periods of 100 s at pressures from 8.5×10^{-10} to 2.8×10^{-6} Torr are shown in Fig. 2. The TPD spectra obtained for D_2 exposure at 120 K appear in Fig. 2a and those for exposure at 200 K in Fig. 2b. The key difference between exposure at these two temperatures is that at 120 K there is no significant dissolution of D atoms into the bulk of the Pd(100) crystal, whereas at 200 K, D atoms are able to dissolve into the Pd(100) bulk [11–14,16,18,19,21,23]. We chose a maximum exposure temperature of 200 K to minimize desorption during the D_2 exposure while allowing bulk dissolution [13]. Consistent with previously published studies [13–19], our TPD spectra display four main features; in increasing order of their peak temperatures, they are labeled α (140 K), $β_1$ (260 K), $β_2$ (305 K), and γ (>305 K). With increasing D_2 exposure, the first TPD feature to appear is $β_2$, followed by γ, $β_1$, and α, in that order.

The $β_2$ feature corresponds to second-order recombinative desorption of D atoms from the Pd(100) surface [13–19]. For low exposures at both 120 K and 200 K, $β_2$ is the only feature that appears, reflecting the stability of surface D atoms at low exposures. The $β_2$ peak maximum, $T_{β2}$, shifts to lower temperatures with increasing exposure, which is typical of a second-order recombinative desorption mechanism. Following the 120 K exposures (Fig. 2a), $T_{β2}$ occurs at ~320 K for the lowest exposure (8.5×10^{-10} Torr for 100 s) and shifts to ~305 K after exposures greater than 1.0×10^{-7} Torr for 100 s. The values of $T_{β2}$ for the two highest exposures at 120 K are identical indicating that the $β_2$ surface state has reached maximum occupancy. This behavior is difficult to observe for exposures at 200 K (Fig. 2b) due to the overlap of the $β_2$ feature with the lower temperature $β_1$ feature. Overlap of features in TPD spectra presents a significant challenge to the analysis of these TPD spectra for kinetic and mechanistic information.

The high temperature tailing edge on the $β_2$ feature is designated γ. The γ feature prevents the observation of a common tailing edge on the $β_2$ feature as would be expected for simple second-order desorption. The γ feature is associated with D diffusion from the Pd bulk to the surface followed by desorption. Other researchers have made this assignment based on the high desorption temperature of the γ feature, its dependence on exposure time, and the observation that it does not saturate with increasing exposure [13–19]. In studies of H_2-TPD from Pd(110) and Pd(100) conducted at hundreds of Langmuir exposure and at temperatures above 300 K, γ has been observed as a prominent feature that is clearly resolved from the $β_2$ feature [13,17]. We observed the γ feature as non-overlapping, high temperature tails on the $β_2$ feature for exposures at both 120 and 200 K, suggesting that diffusion of D into the bulk occurs during heating following low-temperature exposures.

For 100 s exposures at pressures $>5 \times 10^{-9}$ Torr, at both 120 and 200 K, a low-temperature shoulder designated $β_1$, appears on the $β_2$ desorption feature. At these exposures, desorption begins at lower temperatures than expected for a simple recombinative process following the kinetics of the $β_2$ feature. This indicates that the effective activation barrier for desorption of adsorbed D has been lowered. High exposures at 120 K cause only a slight increase in the overall desorption

rate measured at the β_1 and β_2 features (Fig. 2a). In contrast, for exposures at 200 K, the desorption rates for both the β_1 and β_2 features continue to increase with increasing exposure, with the β_1 feature becoming dominant (Fig. 2b). The difference in the growth rate of the β_1 feature for the two exposure temperatures indicates that β_1 occupation is dependent on exposure temperature, which suggests that absorption into the bulk and transport from the bulk of the Pd(100) may play an active role in determining the growth of the β_1 feature. The TPD spectra for the two highest exposures at both 120 K and 200 K display constant values of $T_{\beta 1}$ and $T_{\beta 2}$. This suggests that a first-order mechanism dominates the process and has been ascribed to bulk-to-surface transport [13,14,18].

The α TPD feature only appears following the highest exposure, 2.8×10^{-6} Torr, at 120 K, as shown in Fig. 2a. While the mechanistic details of α desorption remain unclear, Wilde et al. proved that desorption of the α feature occurs concomitantly with depletion of the H concentration in the subsurface region (top ~50 atomic layers). This was demonstrated by correlating the signal from ${}^1H({}^{15}N,\alpha\gamma){}^{12}C$ nuclear reaction analysis with TPD measurements [12,29,30]. H_2 desorption in the α feature has also been observed to have the following general characteristics: the feature only appears for exposure temperatures below 150 K; the desorption mechanism for the α feature shifts from first-order to zero-order kinetics with increasing exposure; the mechanism includes atomic recombination; the peak does not saturate, even at very high exposures; and the magnitude and location of the feature is sensitive to the presence of surface defects and site blocking molecules such as CO [12–14,16,19,21,23,31]. The exposure required to produce the α feature varies among published reports due to the diversity of Pd surfaces, exposure temperatures, and H isotopes used in the studies. However, despite multiple discussions of the feature, there is no consistent mechanistic model that adequately explains how the effective barrier for H recombination and desorption is lowered to allow desorption at temperatures nearly 150 K below those observed for surface recombination (β_2 feature). While hydride phase decomposition seems to be a favored explanation [12–14,16,19,21,23,31], the mechanism still remains to be verified.

The D uptake at 120 and 200 K, estimated from the areas under the TPD spectra, are compared in Fig. 3 as functions of D_2 pressure during a 100 s exposure. The uptake profiles at the two exposure temperatures are nearly identical until they diverge at ~10^{-8} Torr. Similar uptake profiles for low exposures indicate similar uptake rates and suggest surface-only occupation. At 120 K, the rate of D uptake drops considerably for exposures above 1×10^{-8} Torr indicating that there is a substantial barrier to D occupation of the Pd(100) subsurface and the bulk. However, at 200 K, uptake continues for exposures > 10^{-8} Torr indicating that D absorption into the Pd bulk continues as the surface nears saturation.

Our results suggest that uptake and release of D are dependent on both the sample temperature during exposure and the concentration of D in the various occupation sites on the Pd(100) surface and in its bulk. The temperature dependence is reflected in the difference between the high-exposure uptake profiles observed at 120 K and 200 K and the dominance of the β_1 feature in TPD experiments following exposures at 200 K. The divergence in uptake profiles that occurs at ~10^{-8} Torr suggests that at both temperatures, the Pd(100) surface is saturated before population of the subsurface and bulk occurs. At 120 K, the D cannot penetrate deeply into the bulk and so additional exposure results in little net increase in the uptake of D. This was confirmed by the concentration depth profiles measured by Wilde et al. [12]. At 200 K, penetration of D into the subsurface and bulk opens sites on the surface for additional adsorption and uptake of D.

To date, there are no models that have been able to capture all of these features. With the exception of simple surface site-blocking effects, the concentration dependence of the kinetics for penetration of D into the subsurface and bulk has never been introduced into a kinetic model for D or H interactions with Pd. We now turn to a demonstration

that concentration dependence in the kinetic rate constants is an important consideration for modeling the penetration pathways of H or D into the Pd bulk and their release during the TPD experiment.

4. Model, simulation methods, and results

A schematic diagram of the H–Pd system, which defines the distinct occupational regions of the Pd(100) system (surface, subsurface, and bulk), appears in Fig. 1 and was described earlier. A low-coverage, free energy diagram for atomic H on the Pd(100) surface and in the Pd bulk is shown in Fig. 4. The free energy diagram illustrates the relative stabilities of H atoms in the three regions and the barriers to the transport of H atoms between them. For the purposes of this work, the tetrahedral sites are considered to be metastable and the only three stable states considered are the surface hollow, subsurface octahedral site and the bulk octahedral site. The seven primary rate processes in the model are designated by their rate constants: k_{ads} (adsorption), k_{des} (desorption), $k_{S \to SS}$ and $k_{SS \to S}$ (forward and reverse transport between surface (S) and subsurface (SS)), $k_{SS \to B}$ and $k_{B \to SS}$ (forward and reverse transport between the subsurface (SS) and bulk (B)), and bulk diffusion, f_D.

4.1. Rate equations and simulation details

The transport model for D adsorption, absorption and desorption from Pd(100) is based on the description of the D–Pd system as defined in Figs. 1 and 4, and includes three distinct occupation regions (surface, subsurface, and bulk) and seven rate equations. We used density functional theory (DFT), with the generalized gradient approximation, to identify energetically preferred locations of H atoms on the Pd(100) surface and within the Pd(100) subsurface and bulk. Details of the DFT method employed are described in [32,33] and references therein. Our DFT results, which agree with other reports (summarized by Jewell et al. [34]), show that the most stable site on the surface is the fourfold hollow and the most stable site in the subsurface and bulk are octahedral sites. The DFT calculations indicate that D occupation of the top and bridge sites on the (100) surface is significantly less stable than occupation of the fourfold hollow sites. In addition, the tetrahedral sites in the subsurface and bulk are energetically unstable with respect to the hollow site on the surface and octahedral site in the bulk. Therefore, we do not include the top, bridge, or any tetrahedral sites in the model and consider the subsurface to be the first set of octahedral sites below the surface.

We have modeled temporal and spatial changes in D concentration in the various Pd regions using a system of continuum transport equations similar to those described by Mavrikakis et al. [8–10]. The temporal D concentrations in the surface and subsurface domains
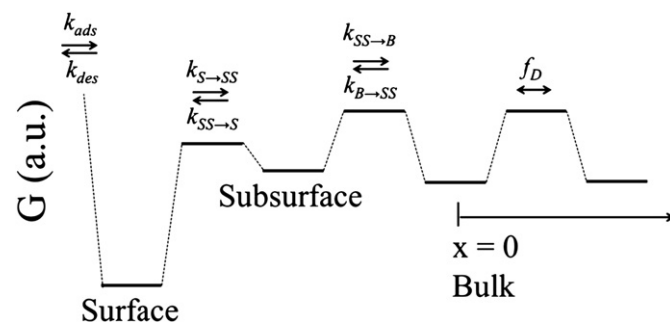

Fig. 4. Free energy diagram showing the approximate stabilities of atomic H in the three primary states and their corresponding rate constants. The seven primary rate processes are indicated by the arrows in the diagram with the respective rate constants. The seven rates constants are adsorption, k_{ads}, desorption, k_{des}, forward and reverse transport between the surface and subsurface, $k_{S \to SS}$ and $k_{SS \to S}$, forward and reverse transport between the subsurface and bulk, $k_{SS \to B}$ and $k_{B \to SS}$, and bulk diffusion, f_D.

are described using ordinary differential equations (ODEs). The spatiotemporal D concentration in the bulk domain is modeled using a one-dimensional partial differential equation (PDE). The ODEs and PDE incorporate transport rate terms, which include rate constants, concentrations of source D atoms, and concentrations of unoccupied sites in the neighboring region. To extend the approach of Mavrikakis et al., we explore how concentration dependent activation barriers influence the overall kinetics of D atom uptake during exposure and D atom release during heating.

The system of equations describing the spatiotemporal changes in concentrations of D in the surface, subsurface, and bulk domains is

$$\frac{d\theta(t)}{dt} = -r_{des} + r_{ads} - r_{S \to SS} + r_{SS \to S}$$
$$\frac{dC_{SS}(t)}{dt} = -r_{SS \to S} + r_{S \to SS} - r_{SS \to B} + r_{B \to SS} \tag{1}$$
$$\frac{\partial C_B(t,x)}{\partial t} = f_D \cdot \frac{\partial^2 C_B(t,x)}{\partial x^2}$$

where x is the direction of D atom transport (normal to the surface plane) and the D concentrations in surface, subsurface, and bulk are $\theta(t)$, $C_{SS}(t)$, and $C_B(t, x)$, respectively. The individual rates, which have been normalized by the site concentrations to give units of s^{-1}, are given as

$$\begin{aligned}
r_{ads} &= k_{ads} \cdot P_{D_2,gas} \cdot (1-\theta(t))^2 \\
r_{des} &= k_{des} \cdot \theta(t)^2 \\
r_{S \to SS} &= k_{S \to SS} \cdot \theta(t) \cdot (1-C_{SS}(t)) \\
r_{SS \to S} &= k_{SS \to S} \cdot C_{SS}(t) \cdot (1-\theta(t)) \\
r_{SS \to B} &= k_{SS \to B} \cdot C_{SS}(t) \cdot (1-C_B(t,x=0)) \\
r_{B \to SS} &= k_{B \to SS} \cdot C_B(t,x=0) \cdot (1-C_{SS}(t))
\end{aligned} \tag{2}$$

The initial conditions at $t = 0$ for the ODEs and PDE, which reflect the state of the system before D_2 exposure are $\theta(0) = 0$, $C_{SS}(0) = 0$, and $C_B(0, x) = 0$. The boundary conditions for the PDE diffusion equation are

$$\frac{\partial C_B(t,0)}{\partial t} = \frac{N_S}{N_B} \cdot (r_{SS \to B} - r_{B \to SS})$$
$$\frac{\partial C_B(t,L)}{\partial x} = 0 \tag{3}$$

where $x = 0$ is the subsurface to bulk boundary, $x = L$ is the thickness of the Pd crystal, N_S is the areal number density of octahedral sites in one atomic Pd layer (6.68×10^{18} m^{-2}), and N_B is the number density of sites in the bulk (1.7×10^{28} m^{-3}).

A number of other assumptions are included in the model: it includes only D motion perpendicular to the surface; it accounts for all interactions by a mean-field treatment; and the Pd metal is assumed to be defect free. The no flux boundary condition at $x = L$ is justified by a simple estimate of the diffusion distance of a D atom through the Pd bulk. The distance that a D atom travels is given by $d = \sqrt{f_D t}$ where f_D is an Arrhenius-like rate constant. The diffusion coefficient for D in Pd has $\Delta E_{diff} = 0.21$ eV and a pre-exponential factor of 1.7×10^{-7} m^2/s [35]. Given these values, D diffuses a distance of ~76 µm in 100 s at 300 K. Our highest exposure temperature was 200 K, so performing this calculation at room temperature provides a conservative estimate of the diffusion distance of D into Pd under the conditions of our experiment. This result justifies the use of the no flux boundary assumption for the ~2.5 mm thick single crystal used in the experiments and the simulation (i.e. $L = 2.5$ mm). This same assumption was used by Mavrikakis et al. [10].

The rate of D release from Pd, which is measured by the QMS during the TPD experiment, is the sum over the derivatives of $\theta(t)$, $C_{SS}(t)$, and $C_B'(t)$ assuming $r_{des} \gg r_{ads}$

$$r_{release} = -\frac{d\theta(t)}{dt} - \frac{dC_{SS}(t)}{dt} - \frac{dC_B'(t)}{dt} \tag{4}$$

where $C_B'(t) = \frac{N_B}{N_S} \int_0^L C_B(t,x)dx$. The assumption is reasonable provided that the pumping speed of the chamber keeps the pressure of D low enough to avoid re-adsorption during the desorption experiment, a normal condition in a TPD experiment.

The simulations account for all independent variables in the TPD experiment including single crystal thickness, Pd temperature, D_2 pressure during exposure, sample cooling during D_2 evacuation, and sample heating during TPD. A key feature of these simulations is that all three experimental stages – exposure, cooling/evacuation, and temperature programmed heating – were incorporated into the model to eliminate the need for assumptions about the D concentration distribution within the Pd immediately following adsorption and prior to TPD. Thus, D concentrations and distributions within each region of the system were never assigned a priori, other than assuming that the concentrations were zero before exposure of the Pd(100) to D_2. Performing the simulation in this way allows the kinetic equations and thermodynamic constants to govern the D distribution during both uptake and release.

The initial gas-phase D_2 pressure and sample temperatures of either 120 K or 200 K during exposure were assigned for each simulation. The initial gas-phase exposure pressure was based on ion-gauge readings recorded during the experimental exposures (adjusted by the ion-gauge sensitivity factor of 0.35 for D_2). Based on our ability to rapidly pump D_2, the D_2 partial pressure during the cooling and heating stages was assumed to be 10^{-11} Torr. During the 100 s cooling/wait period between the end of the exposure and the initiation of the TPD experiment, the temperature was assumed to decrease at a constant rate from either 120 K or 200 K to 100 K.

The system of equations was solved numerically by means of Matlab and Comsol Multiphysics with the UMFPACK nonlinear solver and variable time step sizes. The discretization of bulk elements in the finite element scheme were defined with a step size gradient where the element size was 10 nm at $x = 0$ and 5 µm at $x = L$.

4.2. Rate constants

The model includes seven rate constants as shown in Fig. 4. The rate constant for transport, $k_{i \to j}$ between the surface, subsurface, and bulk sites is described as

$$k_{i \to j} = \frac{k_B T}{h} \cdot \frac{q_{vib}^\ddagger}{q_{vib,i}} \cdot \exp\left(\frac{-\Delta E_{i \to j}}{k_B T}\right) \tag{5}$$

where $q_{vib,i}$ is the vibrational partition function for D in a stable intermediate state and $q_{vib}^\ddagger$ is the vibrational partition function for D at the saddle point between the stable states (f_D is described in a similar fashion). In Eq. (5) k_B is Boltzmann's constant, h is Planck's constant, and T is temperature. The vibrational partition function was implemented as

$$q_{vib} = \prod_{i=1}^{N} \frac{\exp\left(\frac{-h\nu_i}{2k_B T}\right)}{1 - \exp\left(\frac{-h\nu_i}{k_B T}\right)} \tag{6}$$

where N is the number of vibrational modes (i.e. $N = 2$ for a saddle point and $N = 3$ for stable site). DFT was used to calculate the vibrational frequencies for transport from surface to subsurface, subsurface to bulk, and bulk diffusion. The transition state frequencies were calculated at the saddle points between the surface fourfold hollow, subsurface tetrahedral, subsurface octahedral, bulk tetrahedral, and bulk octahedral sites. The values of the vibrational frequencies for the surface, subsurface, and bulk states are fairly consistent with those of previous reports for H in Pd (after a $\sqrt{2}$ correction for D) [18,19,36–40].

The rate constant for desorption, k_{des}, as described by the translational, vibrational, and rotational partition functions is

$$k_{des} = \frac{2S_0 a_s k_B T}{h} \cdot \frac{q_{rot} \cdot q_{vib}}{\left(\lambda \cdot q_3^{ads}\right)^2} \cdot \exp\left(\frac{-\Delta E_{des}}{k_B T}\right), \tag{7}$$

where S_0 is the sticking coefficient; a_s is the area of surface hollow adsorption site; q_{rot} is the gas phase rotational partition function for D_2; q_{vib} is the gas-phase vibrational partition function; q_3^{ads} is the vibrational partition function for adsorbed D atoms where the subscript indicates the three vibrational degrees of freedom on the surface hollow site; and $\lambda = h/\sqrt{2\pi m k_B T}$ is the thermal wavelength with mass, $m = 3.32 \times 10^{-27}$ kg for D. The vibrational and rotational partition functions are given as

$$q_{vib}(T) = \frac{1}{2\sinh\left(\frac{T_{vib}}{2T}\right)} \tag{8}$$

$$q_{rot}(T) = \sum_{j(\text{even})} (2j+1)\exp\left(\frac{-j(j+1)T_{rot}}{T}\right) + 3\sum_{j(\text{odd})} (2j+1)\exp\left(\frac{-j(j+1)T_{rot}}{T}\right) \tag{9}$$

where $q_{rot}(T)$ is separated into para- (odd) and ortho- (even) contributions [41]. The vibrational and rotational partition functions, as functions of temperature, are determined using their respective characteristic vibrational and rotational temperatures of gas-phase molecular D_2: $T_{rot} = 42.9$ K and $T_{vib} = 4305.9$ K [41].

The rate constant for adsorption is given as

$$k_{ads} = \frac{2S_0 a_s \lambda}{h} \tag{8}$$

where k_{ads} has no exponential dependence because adsorption onto the Pd surface is non-activated [42].

4.3. Approaches for defining activation barriers

The model includes activation barriers for each of the seven rate constants: adsorption is non-activated, $\Delta E_{ads} = 0$; desorption, ΔE_{des}; transport from surface to subsurface, $\Delta E_{S \to SS}$; subsurface to surface, $\Delta E_{SS \to S}$; subsurface to bulk, $\Delta E_{SS \to B}$; bulk to subsurface, $\Delta E_{B \to SS}$; as well as bulk diffusion, ΔE_{diff}. As we will demonstrate, the ability of the model to reproduce measured (TPD) release rates depends on the functional forms of the ΔE's dependence on site occupancy. In this section we describe the three forms given by model hypotheses: $\mathcal{H}_1, \mathcal{H}_2$ and $\mathcal{H}_3$.

Our first hypothesis, $\mathcal{H}_1$, assumes constant values of the activation barriers (i.e. $\Delta E = \Delta E^0$, the low-concentration value). This approach is equivalent to most others described in the literature and cited above.

Several published reports indicate that the elementary steps for H atom transport on Pd are sensitive to the concentrations of H/D in the near surface Pd regions. Such sensitivity is attributed to H atom induced lateral distortion (intralayer relaxation) and plane-to-plane separation (interlayer relaxation) [19,25,27,28], as well as thermodynamic phase transitions [23]. A transition between solid solution of H in Pd and Pd-hydride is well-known [35,43] and a decomposing Pd-hydride phase is often considered during H/D release from Pd at low temperatures [12,14,16,19,21,23]. Given this potential for concentration dependent transport coefficients, we have tested two additional hypotheses, $\mathcal{H}_2$ and $\mathcal{H}_3$, that incorporate concentration dependence into our model. These two models extend the constant ΔE model, $\mathcal{H}_1$, by including surface and subsurface concentration effects. The concentration-dependent ΔE terms are applied to transport processes in both directions across the surface to subsurface interface, $\Delta E_{S \to SS}(\theta)$ and $\Delta E_{SS \to S}(\theta)$, and across the subsurface to bulk interface, $\Delta E_{SS \to B}(C_{SS})$ and $\Delta E_{B \to SS}(C_{SS})$. No

concentration dependence was assumed for ΔE_{diff} because of the low D concentrations in the bulk domain.

The model hypothesis $\mathcal{H}_2$ incorporates a linear dependence of the ΔE's on concentrations; for example, the surface to subsurface transition state barrier is described as

$$\Delta E_{S \to SS} = \Delta E_{S \to SS}^0 + \alpha_{S \to SS} \cdot \theta \tag{9}$$

where $\Delta E_{S \to SS}^0$ is the surface to subsurface barrier in the limit of low coverage and $\alpha_{S \to SS}$ defines the sensitivity to D coverage on the surface. This functional form is commonly used to describe the effects of lateral interactions of adsorbed surface species.

The model hypothesis $\mathcal{H}_3$ incorporates concentration dependence in a nonlinear form

$$\Delta E_{S \to SS} = \Delta E_{S \to SS}^0 + \alpha_{S \to SS} \cdot \left(1 - \exp\left(\frac{-\theta^2}{\omega_{S \to SS}}\right)\right) \tag{10}$$

where $\omega_{S \to SS}$ defines the range over which the concentration effects manifest themselves. Examples of the proposed forms for ΔE are illustrated in Fig. 5 as functions of concentration, C, for an arbitrary species. All forms have $\Delta E(C=0) = \Delta E^0$; ΔE for both $\mathcal{H}_2$ and $\mathcal{H}_3$ change by an amount α as $C: 0 \to 1$, provided that $\omega_{S \to SS} \ll 1$. The figure shows that the nonlinear form, described by Eq. (10), allows ΔE to change over a narrow range of concentration and the location of the inflection point to be adjusted with respect to concentration. These two features share behaviors that are characteristic of phase transitions: a phase boundary that is a function of concentration, temperature, and volume, and exhibits discontinuous changes in properties when moving across the boundary.

Our experimental results also suggest that we must modify the barrier for desorption, ΔE_{des}, to describe the α TPD feature which occurs at temperatures nearly 150 K below the β_2 feature. The α TPD feature only occurs for the highest D uptakes and under conditions in which the subsurface contains significant concentrations of D. To account for the low temperature α TPD feature, we include in ΔE_{des} a dependence on surface D coverage (θ), and subsurface D concentration (C_{SS}). Interlayer relaxations and a possible Pd–D phase formation in the near surface region could cause subsurface D to indirectly influence the desorption barrier. Our DFT results suggest, however, that direct interactions between D in the surface and subsurface are too small to impart a 150 K shift in the TPD spectra. In fact, the interaction energy predicted by DFT between D in the surface hollow and subsurface octahedral site was within the error of the DFT method. To represent the influence
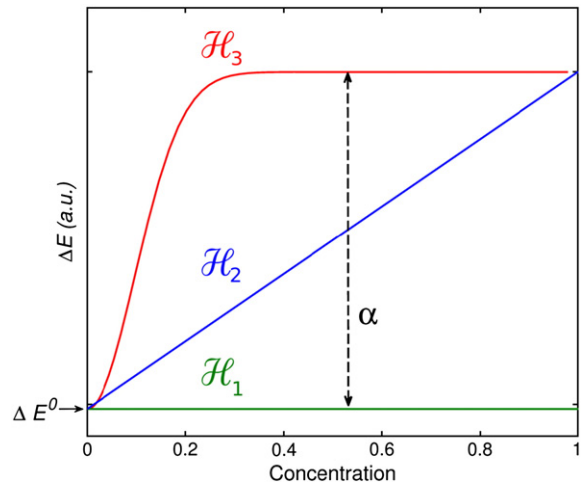

Fig. 5. Proposed forms for the activation barriers (ΔE) versus concentration of an arbitrary species, C. The three forms represent various representations of concentration dependence: constant ($\mathcal{H}_1$), linear ($\mathcal{H}_2$), and nonlinear ($\mathcal{H}_3$). All forms reach a low-concentration limit ($C=0$) at ΔE_{act}^0. Both linear and nonlinear models increase by an amount α at $C=1$.

of subsurface D on the desorption activation barrier, we use the following forms, similar to those in Eqs. (11) and (12),

$$\Delta E_{des} = \Delta E_{des}^0 + \alpha_{des,S} \cdot \theta + \alpha_{des,SS} \cdot C_{SS} \tag{11}$$

$$\Delta E_{des} = \Delta E_{des}^0 + \alpha_{des,\theta} \cdot \left(1 - \exp\left(\frac{-\theta^2}{\omega_{des,\theta}}\right)\right) \tag{12}$$
$$+ \alpha_{des,C_{SS}} \cdot \left(1 - \exp\left(\frac{-C_{SS}^2}{\omega_{des,C_{SS}}}\right)\right)$$

for $\mathcal{H}_2$ and $\mathcal{H}_3$, respectively.

In the next section we compare the predictions of D release kinetics by the three models with three experimental TPD spectra obtained following exposure of the Pd(100) surface to D_2 at 4×10^{-9} and 2.8×10^{-6} Torr at 120 K and 1.4×10^{-6} Torr at 200 K. This group of spectra spans the entire pressure range explored in the experiments, includes both exposure temperatures, and displays all four primary spectral features discussed in Section 3. We perform nonlinear regression on these three spectra in order to optimize the model parameters. The simulations also estimate uptake of D into each of the three Pd regions — surface, subsurface, and bulk.

5. Simulation results and discussion

5.1. Constant ($\mathcal{H}_1$) and linear ($\mathcal{H}_2$) activation barriers

Model $\mathcal{H}_1$ provides a description of the D–Pd(100) system that is similar to that used by Mavrikakis et al. [8–10]. The pre-exponents for the rate constants were estimated using statistical mechanics expressions that used parameters for gas-phase D_2 and vibrational frequencies predicted by DFT for D atoms on or in Pd; these parameters are shown in Table 1. The tunable parameters in the model include six activation barriers, and a sticking coefficient, S_0. $\mathcal{H}_2$ has five more fitting parameters than $\mathcal{H}_1$ — the α_i parameters that describe the linear dependence of the barriers on coverage (i.e. Eqs. (9) and (11)).

Table 1
Best-fit values based on minimizing the sum-squared errors of D_2 TPD spectra based on $\mathcal{H}_3$. S, SS, and B correspond to parameters relating to the surface, subsurface, and bulk. ΔE^0 is an activation barrier at low coverage; S_0 is the sticking coefficient; α represents the amount the barrier changes with changes in D concentrations; ω describes the concentration window which the concentration effects manifest themselves; the real vibrational frequencies, v_i, for D occupying the surface hollow (S), subsurface octahedral (SS), and bulk octahedral (B), and the saddle point transition states (TS) between the S-SS states, SS-B states, and bulk diffusion states. The σ_i represent 95% confidence intervals.

Parameter	φ_i	$\ln(\varphi_i)$	$\ln(\sigma_i)$	DFT vibrational frequency (meV)	
ΔE_{des}^0 (eV)	0.42	−0.86	−0.003	S: v_i	44.3
$\Delta E_{S \to SS}^0$ (eV)	0.40	−0.92	−0.003		44.3
$\Delta E_{SS \to S}^0$ (eV)	0.11	−2.20	−0.08		46.5
$\Delta E_{SS \to B}^0$ (eV)	0.46	−0.77	−0.05	SS: v_i	40.0
$\Delta E_{B \to SS}^0$ (eV)	0.24	−1.43	−0.04		40.0
ΔE_{Diff}^0 (eV)	0.28	−1.27	−0.12		63.9
S_0	0.18	−1.71	−0.04	B: v_i	41.4
$\alpha_{des,\theta}$ (eV)	0.03	−3.67	−0.12		41.4
$\alpha_{des,C_{SS}}$ (eV)	0.74	−0.29	−0.23		27.5
$\alpha_{S \to SS}$ (eV)	0.08	−1.84	−0.11	S-SS TS: v_i	108.6
$\alpha_{SS \to S}$ (eV)	0.16	−1.73	−0.12		82.1
$\alpha_{SS \to B}$ (eV)	0.18	−2.49	−0.09	SS-B TS: v_i	89.5
$\alpha_{B \to SS}$ (eV)	0.01	−5.48	−0.22		92.5
$\omega_{S \to SS}$	4.2×10^{-3}	−8.50	−0.03	B TS: v_i	89.5
$\omega_{SS \to S}$	2.0×10^{-4}	−3.94	−0.19		92.5
$\omega_{SS \to B}$	2.2×10^{-2}	−6.12	−0.24		
$\omega_{B \to SS}$	9.5×10^{-2}	−2.75	−0.22		
$\omega_{des,\theta}$	2.2×10^{-3}	−4.65	−3.64		
$\omega_{des,C_{SS}}$	6.4×10^{-2}	−4.79	−1.06		

The predicted D_2 TPD spectra (solid lines) and the experimental TPD spectra (dots) are shown in Fig. 6(a) and (b), for $\mathcal{H}_1$ and $\mathcal{H}_2$ respectively. The three spectra in each figure correspond to exposures of D_2 at 2.0×10^{-9} and 2.8×10^{-6} Torr for 100 s at 120 K, and an exposure at 1.42×10^{-6} Torr at 200 K for 100 s. A comparison of the total uptake for the experiment and for the predictions of $\mathcal{H}_1$ and $\mathcal{H}_2$ is shown in Fig. 7 for the highest exposures performed at 120 K (2.8×10^{-6} Torr for 100 s) and at 200 K (1.42×10^{-6} Torr for 100 s). The blue, green, and orange regions in the bars represent the predicted occupation of the surface, subsurface, and bulk sites in concentration units given by the amount of D that would occupy one atomic layer of octahedral Pd sites (one monolayer). The experimental uptakes are normalized with the area of the simulated, low-concentration TPD spectrum from the 120 K exposure (uptake not shown).

The limitations of $\mathcal{H}_1$ and $\mathcal{H}_2$ are manifested by their inability to predict all of the desorption features in the TPD spectra (Fig. 6a and b) and the differences between the predicted and experimental D uptakes (Fig. 7). The TPD spectra shown in Fig. 6a illustrate that, while $\mathcal{H}_1$ predicts both the peak desorption temperature for the β_2 feature, $T_{\beta 2}$, and the presence of the γ feature, characterized by non-overlapping high temperature tails, it does not predict the α and β_1 TPD features. The apparent presence of only two simulated spectra is a result of overlapping TPD spectra predicted for the high exposures at 120 and 200 K. Overlap of the spectra means that $\mathcal{H}_1$ predicts identical D uptake – one
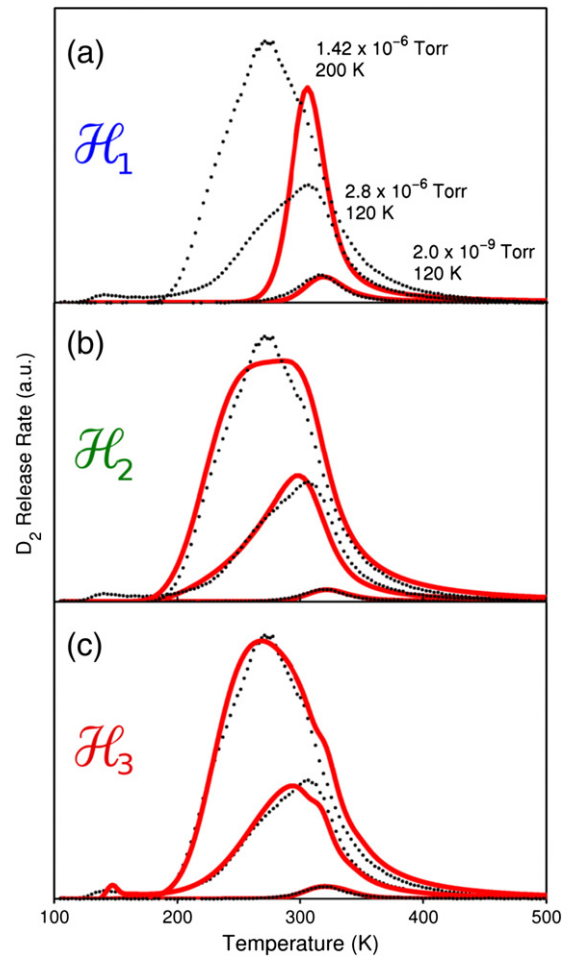

Fig. 6. Experimental TPD (dotted line) plotted against simulated TPD (solid line) for the three hypotheses: (a) constant activation barriers ($\mathcal{H}_1$), (b) linear coverage-dependent activation barriers ($\mathcal{H}_2$), and (c) nonlinear coverage-dependent activation barriers ($\mathcal{H}_3$). The three spectra correspond to two exposures at 120 K: 2.0×10^{-9} and 2.8×10^{-6} Torr for 100 s and one exposure at 200 K: 1.42×10^{-6} Torr for 100 s. The TPD were performed at 3 K/s after cooling to 100 K. The figures indicate that $\mathcal{H}_1$ predicts the β_2 and γ features, $\mathcal{H}_2$ predicts the β_1, β_2 and γ features, and $\mathcal{H}_3$ predicts α, β_1, β_2 and γ features.

monolayer residing on the surface – for both the 120 K and the 200 K exposures. The surface-only occupation is also shown by the predicted concentration distribution in Fig. 7. The experimental data reveal, however, that the uptake of D by Pd(100) is greater than one monolayer, indicating that both adsorption and absorption must occur during these exposures.

The predicted occupation of surface states only is a manifestation of $\mathcal{H}_1$'s primary limitation: with the constant activation barriers, D uptake is controlled by either surface- or bulk-based kinetics; that is, there is either surface-only occupation, or the surface is negligibly occupied and bulk uptake dominates. The 'best-fit' spectra shown in Fig. 6a corresponds to the former. The experimental behavior exhibited by the uptake versus exposure results (c.f. Fig. 3) suggests that a transition between the two uptake regimes takes place during exposure. Only the surface is populated for low exposures, but is followed by uptake into the bulk at high exposures. The uptake into the bulk increases with increasing temperature. We found that there are no choices of optimized barriers which allow $\mathcal{H}_1$ to exhibit this behavior.

In Fig. 6b, the TPD simulations (solid line) based on the model $\mathcal{H}_2$ are compared to the three experimental spectra (dots) obtained following the same exposures as used above. $\mathcal{H}_2$ predicts the appearance of the β_1, β_2, and γ features of the experimental TPD spectra. The presence of the β_1 feature in the TPD spectra predicted by $\mathcal{H}_2$ arises from the higher subsurface and bulk uptake as illustrated in Fig. 7. The prediction of significant subsurface and bulk uptake and the β_1 desorption feature represent improvements over $\mathcal{H}_1$. Nevertheless, $\mathcal{H}_2$ fails to accurately predict the presence of the α TPD feature and the shapes of the β_1 and β_2 features, and it over-predicts uptake for both exposures.

The inability of $\mathcal{H}_1$ and $\mathcal{H}_2$ to accurately predict the α, β_1, and γ features implies that the interactions between the surface and subsurface D, which influence the penetration pathways, are imperfectly described by both $\mathcal{H}_1$ and $\mathcal{H}_2$. Given the poor prediction of uptake and release trends, the constant activation barrier ($\mathcal{H}_1$) and linear concentration dependent ($\mathcal{H}_2$) models are deemed inappropriate for describing the D–Pd(100) system.

5.2. Nonlinear activation barriers ($\mathcal{H}_3$)

We improve upon $\mathcal{H}_1$ and $\mathcal{H}_2$ by introducing a nonlinear dependence of the activation barriers on concentrations in $\mathcal{H}_3$ (c.f. Eqs. (10) and (12)). To account for nonlinearity, six additional parameters were
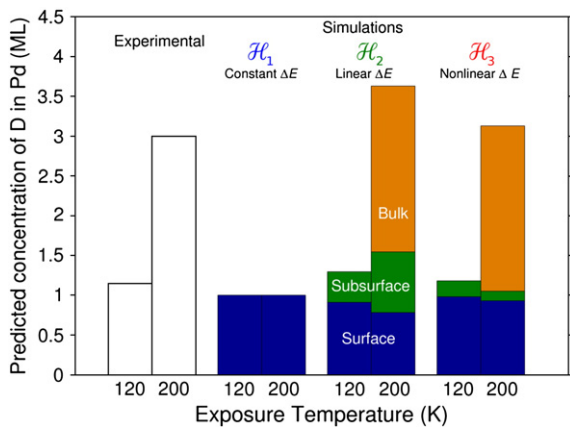
required: $\omega_{S \to SS}$, $\omega_{SS \to S}$, $\omega_{B \to SS}$, and $\omega_{SS \to B}$ for the transport steps, and $\omega_{des,\theta}$ and $\omega_{des,C_{ss}}$ for desorption. The impact of introducing the nonlinear concentration dependence is illustrated by the predicted TPD spectra in Fig. 6c and the uptake in Fig. 7.

The quality of the TPD predictions made using $\mathcal{H}_3$ is demonstrated by Fig. 6c, in which the simulation (solid line) is plotted with the experimental spectra (dots). The simulated spectra exhibit the α, β_1, β_2, and γ features, correct values of T_p, and peak widths that are similar to those of the experiments. $\mathcal{H}_3$ is the only model to predict the α TPD feature with the 120 K exposure and to display the correct shape of the β_1 feature for the 200 K exposure. Fig. 7 provides a comparison of the D uptake predicted by $\mathcal{H}_3$ with the experimental results, and the predictions of $\mathcal{H}_1$ and $\mathcal{H}_2$. Using $\mathcal{H}_3$ the total uptake predictions closely match the experimental results and are improved over those of $\mathcal{H}_2$. Note that the subsurface concentrations predicted by $\mathcal{H}_3$ are significantly lower than those predicted by $\mathcal{H}_2$.

Our results illustrate that among the models tested, $\mathcal{H}_3$ predicts the TPD spectra most accurately, yet the price of a better fit is increased complexity (i.e. additional fitting parameters). An important question is whether the additional complexity results in a statistically significant improvement in the model's predictive capability. Using Bayesian model selection techniques [44,45] we determined that the weight of evidence for the more complex $\mathcal{H}_3$, and against $\mathcal{H}_2$ and $\mathcal{H}_1$, is very strong.

Bayesian hypothesis selection methods were used to evaluate the evidence in favor of model $\mathcal{H}_3$. We use the Bayes factor, S_{ij}, which is a measure of the evidence provided by a data set in favor of one scientific hypothesis, i, over another, j. The Schwartz criterion provides an approximation to the $\log_{10}$ of the Bayes factor as

$$S_{ij} \approx \frac{1}{2}\left(C_{j,0} - C_{i,0}\right) + \frac{1}{2}\left(N_j - N_i\right)\log_{10}M \tag{13}$$

where $C_{i,0}$ is the ground state cost (minimum sum of squared errors) of a model i, N_i is the number of parameters in model i, and M is the number of measurements that were used in calculating the cost function [44]. Conclusions are drawn based on the magnitude of S_{ij}: 0–0.5 (inconclusive), 0.5–1 (positive), 1–2 (strong), and >2 (decisive) [45].

In our selection tests, a total of 1475 measurements from twelve TPD spectra chosen from the 120 K and 200 K exposure experiments were used to calculate the lowest cost. Each measurement corresponds to a single data point. The number of parameters for $\mathcal{H}_1$, $\mathcal{H}_2$, and $\mathcal{H}_3$ were 7, 13, and 19, respectively. S_{21} and S_{32} were determined to be 6.8 and 7.6, respectively. This analysis shows that the weight of evidence for the more complex $\mathcal{H}_3$ is decisive. Furthermore, it suggests that nonlinear concentration dependent activation barriers are warranted for an accurate description of D_2 release from Pd(100).

5.3. D distribution in Pd(100)

Concentration profiles versus temperature, which were generated from the model $\mathcal{H}_3$ provide insight into the initial distribution of D atoms in the Pd(100) system after exposure and the redistribution within the system that takes place as the TPD experiment proceeds. Fig. 8 displays the experimental and simulated TPD spectra and the simulated concentration profiles versus temperature for the total D concentration, θ, C_{SS}, and C'_B. Fig. 8a represents the TPD following the 2.8×10^{-6} Torr exposure of D_2 to Pd(100) at 120 K; Fig. 8b represents the TPD following the 1.4×10^{-6} Torr exposure of D_2 to Pd(100) at 200 K. The concentrations profiles for the 120 K and 200 K simulations are shown in Fig. 8(c) and (d), respectively. The initial concentration values in each figure match those shown in Fig. 7. The surface is almost saturated at both exposure temperatures and the subsurface has 0.21 and 0.12 ML for the 120 K and 200 K exposures, respectively. The primary difference between the distributions of D in Pd(100) following adsorption and absorption at 120 K and 200 K is the concentration in the bulk, C'_B. There is a significant population
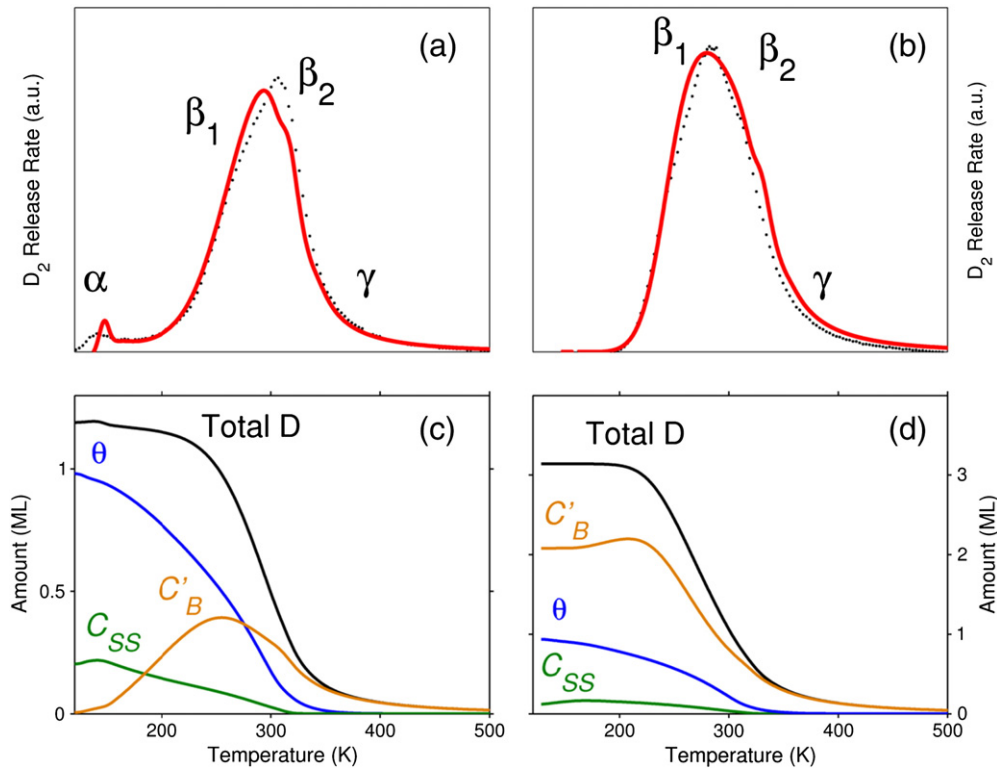

Fig. 7. Bar graph showing the experimental and simulated D uptake for 2.8×10^{-6} and 1.42×10^{-6} Torr exposures at 120 and 200 K. Predicted D concentration in surface (θ), subsurface (SS), and bulk (B) domains are shown for the simulated bars. Only the total concentration for experimental results is shown. Each bar in the plot reflects the total uptake at the given temperature with sections corresponding to the distribution in the specific domains for surface (lowest region — blue), subsurface (middle region — green), and bulk (highest region — orange).

Fig. 8. Experimental and simulated TPD spectra (top panel) and simulated concentration profiles (bottom panel) for the total D concentration, surface concentration ($\theta(t)$), subsurface concentration ($C_S(t)$), and bulk concentration ($C'_B(t)$) where $C_{B'}(t) = N_B/N_S \int_0^L C_B(t,x)dx$. TPD corresponds to (a) 2.8×10^{-6} Torr exposure of D_2 at 120 K and (b) 1.4×10^{-6} Torr exposure of D_2 at 200 K to Pd(100) with a 3 K/s heating rate.

of D in the bulk following exposure at 200 K, but almost no D in the bulk following exposure at 120 K.

D_2 desorption exhibits a low temperature α TPD feature only after the 120 K exposure; the model TPD spectrum shows the increase in the desorption rate paralleled by a decrease in the total amount of D, that is, both θ and C_{SS}. This behavior is not observed with the 200 K exposure — the total D concentration remains constant until $T = \sim 240$ K. While the two systems have different amounts of C'_B after exposure, as the temperature increases, C'_B increases in both Fig. 8(a) and (b). Comparison of C'_B and the α TPD feature in Fig. 8a shows that C'_B increases just as the α TPD feature begins to decrease. The inverse changes observed for C'_B and the α TPD feature suggest that the propensity to move into the bulk becomes greater than the propensity to desorb. This also implies that the interactions included in our effective desorption barrier are only operative at low temperatures when mobility in the bulk is low and D concentrations in the subsurface region reach sufficiently high levels.

As the temperature increases, C'_B continues to increase for both systems and reaches a maximum near 240 K of ~0.4 and ~2.25 equivalent MLs, for the 120 and 200 K experiments, respectively. Fig. 8(a) and (b) shows that the desorption rate – after both 120 and 200 K exposures – rapidly increases when C'_B reaches this maximum concentration. The increase in the desorption rate with a decrease in C'_B suggests that the remaining desorption features – β_1, β_2, and γ – are influenced by a sequence of diffusive transport from the bulk states, passage through the subsurface, and desorption from the surface. Both the 120 K and the 200 K concentration profiles also show an overlap of C'_B with the total D concentration at temperatures above ~350 K — an indication that the γ feature is directly related to D release from the bulk. We can infer, therefore, that multiple steps influence the desorption kinetics of the β_1, β_2, and γ features. Of course, a complete analytical methodology such as the degree of rate control described by Campbell et al. [46] should be used to determine which steps are rate-limiting or inhibiting in the evolution of gas-phase D_2.

5.4. Best-fit parameter values and sensitivity

The best-fit parameters for the low-concentration limit activation barriers, the sticking coefficient, and parameters (α and ω) describing the concentration dependence of the transport and desorption barriers, are shown in Table 1. The table also lists the real vibrational frequencies, v_i, determined from DFT: three for each normal mode in the stable intermediate states (S, SS, and B), and two normal modes for each transition state (S-SS, SS-B, and bulk diffusion).

Values for activation barriers on the various Pd faces have been reported in the literature: ΔE_{des} ranges from 0.80 to 1.10 eV [3–5,11, 15,39,47–50]; $\Delta E_{S \rightarrow SS}$ ranges from 0.05 to 0.57 eV [4,5,10,11,14,23, 25,39,51–56]; $\Delta E_{SS \rightarrow S}$ ranges from 0.04 to 0.33 eV [10,14,16,23, 50,54,55,57]; $\Delta E_{SS \rightarrow B}$ ranges from 0.09 to 0.52 eV [10,14,23,54]; $\Delta E_{B \rightarrow SS}$ ranges from 0.22 to 0.44 eV [4,5,10,54]; and ΔE_{diff}^0 ranges from 0.20 to 0.23 [35,58,59]. Only ΔE_{diff}^0 has been determined using a variety of both theoretical and experimental methods. The remaining barriers have been inferred using either basic analyses of TPD spectra or from theoretical modeling. The large spread in the reported values for the surface-subsurface-bulk barriers reflects the reality that multiple theoretical approaches were used. Even state of the art DFT methods have delivered a wide range of predictions for the H–Pd system, many of which have been inconsistent with experimental results [34]. The variation in the parameters results from various lattice constants of Pd, which come from alternative descriptions of the electron–electron interactions in DFT. Furthermore, differences also arise from different H concentrations used in these calculations [37,40,60]. Regardless, our activation barriers for the low concentration limit – shown in Table 1 – all lie within the cited ranges.

Very few studies have reported concentration-dependent barriers for H transport between the surface, subsurface, and bulk. Two different reports suggest that $\Delta E_{S \rightarrow SS}$ changes by -0.17 [37] and -0.19 eV [55] as H concentrations change. The authors of those studies have suggested that H-induced intralayer relaxations of the Pd lattice are

responsible for these changes in $\Delta E_{S \to SS}$. They also suggest that this relaxation changes the surface hollow binding energy by 0.10 eV with concentrations of 0.25 to 1 ML in the Pd subsurface. Furthermore, the authors argue that the H binding energy in the octahedral subsurface sites changes by -0.20 eV following interlayer relaxations of the Pd lattice [28,37]. The concentration dependence of these intermediate and transition state energies will have an effect on $\Delta E_{SS \to S}$ and $\Delta E_{SS \to B}$, and ΔE_{des}. The magnitude and direction of change (increase or decrease in energy) predicted by our model is consistent with these reports.

The sensitivity of a model defines the uncertainty of parameters estimated using that model; a small uncertainty for a given parameter indicates that the predictions of the model are sensitive to its value. On the other hand, if the uncertainty in the parameter is large, the predictions of the model are not sensitive to its value. The 95% confidence limit for each parameter, σ_i, was calculated from the Hessian about the best-fit values of the parameters as $\sigma_i = \sqrt{\left(H_{ij}^{-1}\right)_{i=j}}$. This relationship holds because the inverse of the Hessian is equal to the covariance matrix [61]. Each optimized parameter and its natural logarithm, $\ln(\varphi_i)$ and the natural log of the confidence limits, $\ln(\sigma_i)$, determined from $\mathcal{H}_3$ are shown in Table 1.

Finally, we must make clear that one of our principle assumptions was that the concentration changes affected only the enthalpy part of the free energy barriers; we did not consider entropic dependence on concentration even though many physical effects, such as lattice relaxations, could affect H vibrations and the curvature of the energy hypersurface.

6. Concluding remarks

The uptake and release of hydrogen by Pd was modeled for the first time using concentration-dependent activation barriers and a description of the systems that included adsorption, absorption and release of hydrogen during isothermal exposure to D_2 followed by subsequent heating. We have shown that nonlinear concentration dependent activation barriers are consistent with previous understanding of the complex Pd–H system and that they accurately predict – over a wide temperature and pressure space – multiple desorption features observed in TPD experiments. The model will be useful in further studies which are directed toward understanding the degree to which each of the various rate elementary processes control the evolution of hydrogen in the four features observed in the TPD spectra of D_2 from a Pd(100) surface exposed to D_2 at elevated temperatures and pressures.

References

[1] D.S. Sholl, J. Alloys Compd. 446 (2007) 462.
[2] A. Pisarev, J. Membr. Sci. 335 (2009) 51.
[3] C. Ling, D.S. Sholl, J. Membr. Sci. 303 (2007) 162.
[4] T.M. Ward, T. Dao, J. Membr. Sci. 153 (1999) 211.
[5] I.J. Iwuchukwu, A. Sheth, Chem. Eng. Process. 47 (2008) 1298.
[6] B.D. Morreale, B.H. Howard, O. Iyoha, R.M. Enick, C. Ling, D.S. Sholl, Ind. Eng. Chem. Res. 46 (2007) 6313.
[7] A. Borgschulte, R. Gremaud, R. Griessen, Phys. Rev. B 78 (2008) 094106.
[8] M. Mavrikakis, J.W. Schwank, J.L. Gland, Surf. Sci. 355 (1996) L385.
[9] M. Mavrikakis, J.W. Schwank, J.L. Gland, J. Chem. Phys. 100 (1996) 11389.
[10] M. Mavrikakis, J.W. Schwank, J.L. Gland, J. Chem. Phys. 105 (1996) 8398.
[11] H. Conrad, G. Ertl, E.E. Latta, Surf. Sci. 41 (1974) 435.
[12] M. Wilde, K. Fukutani, Phys. Rev. B 78 (2008) 115411.
[13] G.E. Gdowski, T.E. Felter, R.H. Stulen, Surf. Sci. 181 (1987) L147.
[14] H. Okuyama, W. Siga, N. Takagi, M. Nishijima, T. Aruga, Surf. Sci. 401 (1998) 344.
[15] R.J. Behm, K. Christmann, G. Ertl, Surf. Sci. 99 (1980) 320.
[16] R.J. Behm, V. Penka, M.-G. Cattania, K. Christmann, G. Ertl, J. Chem. Phys. 78 (1983) 7486.
[17] M.G. Cattania, V. Penka, R.J. Behm, K. Christmann, G. Ertl, Surf. Sci. 126 (1983) 382.
[18] D. Farias, P. Schilbe, M. Patting, K.H. Rieder, J. Chem. Phys. 110 (1999) 559.
[19] U. Muschiol, P.K. Schmidt, K. Christmann, Surf. Sci. 395 (1998) 182.
[20] G. Rupprechter, M. Morkel, H.J. Freund, R. Hirschl, Surf. Sci. 554 (2004) 43.
[21] G. Rupprechter, M. Morkel, H.J. Freund, Surf. Sci. 588 (2005) L209.
[22] C. Langhammer, V.P. Zhdanov, I. Zoric, B. Kasemo, Phys. Rev. Lett. 104 (2010).
[23] G. Rupprechter, M. Morkel, H.J. Freund, R. Hirschl, Surf. Sci. 554 (2004) 43.
[24] H. Okuyama, T. Nakagawa, W. Siga, N. Takagi, M. Nishijima, T. Aruga, Surf. Sci. 428 (1999) 277.
[25] R.A. Olsen, G.J. Kroes, E.J. Baerends, J. Chem. Phys. 109 (1998) 2450.
[26] S.W. Rick, D.L. Lynch, J.D. Doll, J. Chem. Phys. 99 (1993) 8183.
[27] E.C.H. Sykes, L.C. Fernandez-Torres, S.U. Nanayakkara, B.A. Mantooth, R.M. Nevin, P.S. Weiss, Proc. Natl. Acad. Sci. U. S. A. 102 (2005) 17907.
[28] O.M. Lovvik, R.A. Olsen, J. Chem. Phys. 104 (1996) 4330.
[29] K. Christmann, Surf. Sci. 603 (2009) 1405.
[30] M. Wilde, M. Matsumoto, K. Fukutani, T. Aruga, Surf. Sci. 482–485 (2001) 346.
[31] D. Farias, M. Patting, K.H. Rieder, Phys. Status Solidi A: Appl. Res. 159 (1997) 255.
[32] D.R. Alfonso, Surf. Sci. 600 (2006) 4508.
[33] J.B. Miller, D.R. Alfonso, B.H. Howard, C.P. O'Brien, B.D. Morreale, J. Phys. Chem. C 113 (2009) 18800.
[34] L.L. Jewell, B.H. Davis, Appl. Catal. A: Gen. 310 (2006) 1.
[35] Y. Fukai, The Metal–Hydrogen System: Basic Bulk Properties, 2 ed. Springer, Berlin, 2005.
[36] H. Conrad, M.E. Kordesch, W. Stenzel, M. Sunjic, B. Trninicradja, Surf. Sci. 178 (1986) 578.
[37] O.M. Lovvik, R.A. Olsen, Phys. Rev. B 58 (1998) 10890.
[38] C. Nyberg, C.G. Tengstal, Phys. Rev. Lett. 50 (1983) 1680.
[39] J. Greeley, M. Mavrikakis, J. Phys. Chem. B 109 (2005) 3460.
[40] K.I. Abdallah, S. Mohamed, R. Mohamed, G. Abdelhalim, Acta Crystallogr. Sect. C: Crys. Struct. Commun. 62 (2006) I43.
[41] H.J. Kreuzer, Z. Jun, S.H. Payne, W. Nichtlpecher, L. Hammer, K. Muller, Surf. Sci. 303 (1994) 1.
[42] A. Gross, Surf. Sci. 363 (1996) 1.
[43] G. Alefeld, Phys. Status Solidi 32 (1969) 67.
[44] R.E. Kass, L. Wasserman, J. Am. Stat. Assoc. 90 (1995) 928.
[45] A.E. Raftery, G.H. Givens, J.E. Zeh, J. Am. Stat. Assoc. 90 (1995) 402.
[46] C. Stegelmann, A. Andreasen, C.T. Campbell, J. Am. Chem. Soc. 131 (2009) 8077.
[47] A.W. Aldag, L.D. Schmidt, J. Catal. 22 (1971) 260.
[48] K. Christmann, U. Muschiol, Z. Phys. Chem. Int. J. Res. Phys. Chem. Chem. Phys. 197 (1996) 155.
[49] J.M. Heitzinger, A. Avoyan, B.E. Koel, Surf. Sci. 294 (1993) 251.
[50] W. Dong, V. Ledentu, P. Sautet, A. Eichler, J. Hafner, Surf. Sci. 411 (1998) 123.
[51] S. Wilke, D. Hennig, R. Lober, M. Methfessel, M. Scheffler, Surf. Sci. 309 (1994) 76.
[52] J.-F. Paul, P. Sautet, Phys. Rev. B 53 (1996) 8015.
[53] J.D. Doll, S.W. Rick, D.L. Lynch, Abstr. Pap. Am. Chem. Soc. 206 (1993) 39.
[54] N. Ozawa, N.B. Arboleda, T.A. Roman, H. Nakanishi, W.A. Dino, H. Kasai, J. Phys. Condens. Matter 19 (2007) 365214.
[55] B.S. Kang, K.S. Sohn, Physica B 217 (1996) 160.
[56] S. Hong, T.S. Rahman, Phys. Rev. B 75 (2007) 155405.
[57] P.M. Richards, J. Nucl. Mater. 152 (1988) 246.
[58] G. Alefeld, J. Volkl, Hydrogen diffusion in metals, in: A.S. Nowick, J.J. Burton (Eds.), Diffusion in Solids: Recent Developments, Academic Press, New York, 1975, p. 231.
[59] X.Z. Ke, G.J. Kramer, Phys. Rev. B 66 (2002).
[60] R.A. Olsen, G.J. Kroes, O.M. Lovvik, E.J. Baerends, J. Chem. Phys. 107 (1997) 10652.
[61] K.-V. Yuen, Bayesian Methods for Structual Dynamics and Civil Engineering, John Wiliey & Sons, Singapore, 2010.